RESEARCH ARTICLE | SEPTEMBER 04 2024

A combination of acoustophoresis and thermophoresis for enriching nanoparticles

Jing Dong (董婧) ⬡ ; Dongfang Liang (梁东方) ⬡ ; Alexandre J. Kabla ⬡ ; Xinan Chen (陈浠楠) ⬡ ;
Xin Yang (杨欣) ✉ ⬡

🔴 Check for updates

🌐 View Online

➡ Export Citation

Articles You May Be Interested In
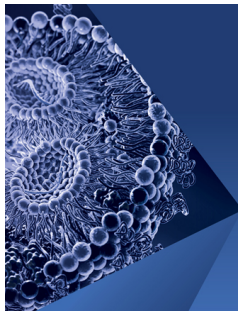
Physics of Fluids

Special Topic:

Flow and Lipid Nanoparticles

Guest Editors: Richard Braatz and Mona Kanso

Submit Today!

AIP Publishing

A combination of acoustophoresis and thermophoresis for enriching nanoparticles

View Online   Export Citation   CrossMark

Jing Dong (董婧),[1] (iD) Dongfang Liang (梁东方),[1] (iD) Alexandre J. Kabla,[1] (iD) Xinan Chen (陈浠楠),[2] (iD)
and Xin Yang (杨欣)[3,a] (iD)

AFFILIATIONS

[1]Department of Engineering, University of Cambridge, Cambridge CB2 1PZ, United Kingdom
[2]International Business School, Xi'an Jiaotong-Liverpool University, Suzhou 215123, China
[3]Department of Electrical and Electronic Engineering, School of Engineering, Cardiff University, Cardiff CF24 3AA, United Kingdom

[a]Author to whom correspondence should be addressed: yangx26@cardiff.ac.uk

ABSTRACT

Over the past few decades, nanotechnology has seen widespread growth in biomedical applications. Recently, thermophoresis has been proposed as an efficient method to manipulate nanoparticles. However, the enrichment time can be quite long due to the associated convection flow. To address this issue, this paper proposes a novel method that combines the deployment of standing surface acoustic waves (SSAW) and temperate gradients for more efficient nanoparticle enrichment. The enrichment system consists of a microchamber sandwiched by a piezoelectrical substrate top slide, from where infrared light laser heat source and SSAW are introduced, and a sapphire bottom. The SSAW-induced thermoacoustic streaming can be properly controlled to partially cancel the effect of natural heat convection, reducing its adverse impact on thermophoresis and consequently reducing the enrichment time. A numerical model is established, which is verified against experimental observation. A parametric study is then undertaken to examine the influence of the acoustic field on the enrichment time with a laser power of 194 mW. The efficiency and suitability of the coupled system depend on the magnitude and direction of SSAW. With the optimized actuation condition, the enrichment time can be reduced by 61% compared to that of the pure thermophoretic enrichment. Finally, different laser powers are considered, ranging from 194 to 248 mW. Again, around 61% time reduction can be achieved in all the tested cases. The optimum magnitude of the acoustic waves slightly increases with the laser power. This innovative enrichment approach is thus demonstrated to be effective.

I. INTRODUCTION

Nanoparticle enrichment plays a crucial role in biomedical research and diagnostics. Previous studies have explored the use of acoustophoresis to manipulate nanoparticles;[1–6] however, precise control over nanoparticle movement can be challenging due to the steep decrease in the acoustic radiation forces as the particle size decreases, which consequently influences particle manipulation efficiency. Existing experiments have also investigated thermophoresis enrichment of nanoparticles,[7,8] demonstrating the ability to enrich exosomes within 10 min using laser heating. In the thermophoresis enrichment process, nanoparticle accumulation is governed by the interplay between thermophoresis and convection induced by localized heating. However, utilizing laser heating alone can result in strong thermal convection, causing particles to circulate within the convection and thereby prolonging the enrichment duration of nanoparticles.[7] It is imperative to develop a more efficient and safer method for nanoparticle enrichment, as this is critically required across various disciplines, including biophysical, biochemical, and biomedical fields. In response to these challenges, this paper presents a novel enrichment method that integrates acoustophoresis and thermophoresis to enhance nanoparticle enrichment efficiency. In our model, in addition to the infrared laser heat source, acoustic waves are introduced at the top of the microchamber. When an acoustic wave is induced in a fluid with a temperature gradient, thermoacoustic streaming can be generated.[9] By properly selecting the acoustic field intensity, the induced thermoacoustic streaming can be effectively controlled to move in the opposite direction of the thermal convection. The thermoacoustic streaming partially cancels the effect of natural heat convection, reducing its adverse impact on thermophoresis and consequently shortening the enrichment time.

30 September 2024 11:24:06

In this research, surface acoustic waves (SAWs) are used in particle enrichment. SAWs are elastic waves that propagate along the surface of a solid material, with their amplitude decaying exponentially with depth into the material.[10] SAWs are generated using interdigital transducers (IDTs) and can manipulate fluids and particles at microscale levels due to their ability to induce acoustic streaming and radiation forces.[11] They have numerous applications in digital acoustofluidics and continuous-flow acoustofluidics due to their advantages, including excellent biocompatibility, simplicity, and contactless manipulation. In digital acoustofluidics, SAWs are utilized for droplet-based applications such as droplet impact actuation and droplet motion, enabling precise control of droplet formation and movement on surfaces.[12–16] Additionally, continuous-flow acoustofluidics has been used effectively for cell sorting and particle focusing within microchannels, enhancing the precision and efficiency of these processes.[17–21]

Some researchers have investigated the underlying physical mechanisms governing the interaction between acoustic and temperature fields at the microscale. In contrast to traditional acoustic fields, one key phenomenon that emerges is thermoacoustic streaming, which occurs when an acoustic wave is induced in a fluid with a temperature gradient. Recently, Qiu *et al.* conducted a comprehensive experimental and numerical study of thermoacoustic streaming in liquids induced by temperature gradients in a microchannel.[22] A theoretical explanation for this phenomenon was also provided, and the acoustic body force acting on the inhomogeneous fluid was introduced.[9,23] Thermoacoustic streaming, driven by the nondissipative acoustic body force, has a markedly different origin compared to conventional acoustic streaming associated with energy dissipation. Furthermore, it reaches much higher velocity amplitudes than boundary-driven Rayleigh streaming and Rayleigh–Bénard convection under comparable conditions. The thermoacoustic streaming effect has been employed to develop an opto-acoustophoretic jet generator for microparticles or cells[24,25] and has been utilized in the manipulation of submicrometric particles down to 500 nm,[26] such as bacteria,[27] as well as in the trapping of hot plasma in gases.[28] Nonetheless, the fundamental physical mechanisms governing the thermoacoustic field remain incompletely understood. The full potential of thermoacoustic streaming applications has yet to be realized, and there has been limited exploration into the integration of thermophoresis and acoustophoresis in nanoparticle enrichment processes.

This work develops a numerical model that integrates acoustophoresis and thermophoresis for nanoparticle enrichment, aiming to enhance the efficiency of the process. The effect of the acoustic field on particle enrichment efficiency is investigated, and the optimum enrichment condition is determined. By testing laser powers ranging from 194 to 248 mW, the variation of optimum acoustic pressure is analyzed. In this work, the finite element method is employed to model the thermoacoustic motion of microparticles in a SAW-driven microchamber. An infrared (IR) laser is used to generate temperature gradients for nanoparticle enrichment. Two pairs of IDTs are placed at the top of the microchamber to generate two SAWs propagating in opposite directions on the substrate. The interference between these SAWs, having the same frequency and amplitude, forms an SSAW on the surface of the piezoelectric substrate.[11] The fluid motion is governed by the continuity, Navier–Stokes and energy equations. Perturbation theory is applied to numerically solve these governing

equations. The first-order solution corresponds to the periodic oscillations, while the second-order solution is related to the acoustic streaming field and temperature field. Various forces, including the thermophoretic, drag, acoustic radiation, lift, Brownian, and buoyancy forces, act on solid particles to drive their motion. To validate this numerical model, an existing experiment from the literature is reproduced.[25] Subsequently, the impact of the acoustic field and its sensitivity to laser powers on nanoparticle enrichment are systematically studied. These findings offer potential applications for thermoacoustic streaming and insight into the design of novel nanoparticle enrichment devices.

II. MATHEMATICAL MODEL
A. Governing equations

In this model, the continuity equation, compressible-flow Navier–Stokes equation, and energy equation are employed as follows:[29–31]

$$\partial_t \rho + \nabla \cdot (\rho \boldsymbol{v}) = 0, \tag{1}$$

$$\partial_t (\rho \boldsymbol{v}) = \nabla \cdot [\boldsymbol{\sigma} - p\mathbf{I} - \rho \boldsymbol{v}\boldsymbol{v}] + \rho \boldsymbol{g}, \tag{2}$$

$$\partial_t \left(\rho \epsilon + \rho \frac{v^2}{2} \right) = \nabla \cdot \left[k\nabla T + \boldsymbol{v} \cdot \boldsymbol{\sigma} - p\boldsymbol{v} - \rho \boldsymbol{v} \left(\epsilon + \frac{v^2}{2} \right) \right] + Q, \tag{3}$$

where $\boldsymbol{v}$ is flow velocity, p is pressure, ρ is density, k is thermal conductivity, $\boldsymbol{g}$ is acceleration due to gravity in the z-axis direction and pointing downwards, ϵ is the internal energy density, T is temperature, and $\mathbf{I}$ is the unit tensor, respectively. The shear stress is

$$\boldsymbol{\sigma} = \mu \left[\nabla \boldsymbol{v} + (\nabla \boldsymbol{v})^T \right] + \left(\mu_b - \frac{2}{3}\mu \right) [\nabla \cdot \boldsymbol{v}]\mathbf{I}, \tag{4}$$

where μ and μ_b are the shear and bulk viscosity coefficients of the fluid.

Pressure p and temperature T are related to the internal energy density ϵ by the first law of thermodynamics and to the density ρ by the equation of state as follows:

$$\rho d\epsilon = (\rho c_p - \alpha_p p)dT + (\kappa p - \alpha_p T)dp, \tag{5a}$$

$$d\rho = -\rho \alpha_p dT + \rho \kappa dp, \tag{5b}$$

where c_p is the constant-pressure heat capacity of the fluid, α_p is the thermal expansion coefficient, and κ is the compressibility of the fluid.

The final term in the energy equation Q represents the power density of an external energy source, which is induced by a flat-top IR laser beam in this study. The external power density is assumed to be constant in the x-axis direction in the working area, while it attenuates in the z-axis direction. The power density distribution of the IR laser in the working area is modeled according to the Beer–Lambert law as follows:[32]

$$Q = Q_{total}/(\pi r_0^2) \times \exp(-(H-z)/\lambda), \tag{6}$$

where Q_{total} is the total laser power, r_0 is the spot radius of the laser, H is the height of the microchamber, the z-axis coordinate is aligned with the centerline of the laser beam, and λ is the attenuation length.

Because of the timescale disparity between the acoustic oscillation and particle motion, Nyborg's perturbation technique is employed to

separate the timescales.[33] The thermoacoustic motion induced by harmonic forcing can be decomposed into two parts: a periodic component with the same period as the acoustic actuation and a second-order component with a non-zero time-averaged motion.[34] Each flow field variable or temperature can be expressed in terms of these three components, i.e., the zeroth-order (or hydrostatic), first-order (harmonic), and second-order (streaming) components,

$$f = f_0 + f_1 + f_2 + \cdots, \tag{7}$$

where f represents $\boldsymbol{v}$, p, and ρ, and the subscripts 0, 1, and 2 represent the zeroth-order (or hydrostatic), first-order (harmonic), and second-order (streaming) components, respectively.

Therefore, based on Eqs. (1)–(3), we can find ρ_0, p_0, $\boldsymbol{v_0}$, and T_0, which describe the steady background field as follows:

$$\nabla \cdot (\rho_0 \boldsymbol{v_0}) = 0, \tag{8a}$$

$$\nabla \cdot [\boldsymbol{\sigma_0} - p_0 \mathbf{I} - \rho_0 \boldsymbol{v_0} \boldsymbol{v_0}] + \rho_0 \boldsymbol{g} = 0, \tag{8b}$$

$$\nabla \cdot \left[k \nabla T_0 + \boldsymbol{v_0} \cdot \boldsymbol{\sigma_0} - p_0 \boldsymbol{v_0} - \rho_0 \boldsymbol{v_0} \left(C_p T_0 + \frac{v_0^2}{2} \right) \right] + Q_0 = 0, \tag{8c}$$

where $Q_0 = Q$ and $\boldsymbol{\sigma_0} = \mu[\nabla \boldsymbol{v_0} + (\nabla \boldsymbol{v_0})^T] + \left(\mu_b - \frac{2}{3}\mu \right)[\nabla \cdot \boldsymbol{v_0}]\mathbf{I}$. By neglecting higher order terms, the following first-order equations can be derived,[35] which specify the harmonic component of the fluid response to the imposed acoustic oscillation. The harmonic time dependence is mathematically expressed as $e^{-i\omega t}$,

$$i\omega \rho_1 = -\rho_0 \nabla \cdot \boldsymbol{v_1}, \tag{9a}$$

$$-i\omega \rho_0 \boldsymbol{v_1} = -\nabla p_1 + \mu \nabla^2 \boldsymbol{v_1} + \left(\mu_b - \frac{2\mu}{3} \right) \nabla(\nabla \cdot \boldsymbol{v_1}). \tag{9b}$$

The first-order fields have a harmonic time dependence; thus, the time average of these fields is zero. Therefore, first-order terms lead to no net fluid motion. The description of non-zero time-averaged flow field thus requires the solution of the second-order equations,[22,36]

$$-\nabla \cdot \langle \rho_1 \boldsymbol{v_1} \rangle = \rho_0 \nabla \cdot \langle \boldsymbol{v_2} \rangle, \tag{10a}$$

$$\nabla \cdot \langle \boldsymbol{\sigma_2} \rangle + \boldsymbol{f_{ac}} = 0, \tag{10b}$$

where the angled bracket $\langle \dots \rangle$ represents the time average of the quantity inside over an oscillation period. The product of the two first-order quantities leads to non-zero average values and that act as the source terms driving the second-order flow field. Physically, the non-zero averaged velocity $\langle \boldsymbol{v_2} \rangle$ corresponds to acoustic streaming. Here, the time-averaged second-order acoustic force density $\boldsymbol{f_{ac}}$ can be defined as the divergence of the time-averaged acoustic momentum flux density tensor,[22]

$$\boldsymbol{\sigma_2} = \mu \left[\nabla \boldsymbol{v_2} + (\nabla \boldsymbol{v_2})^T \right] + \left(\mu_b - \frac{2}{3}\mu \right)(\nabla \cdot \boldsymbol{v_2})\mathbf{I}$$
$$+ \mu \left[\nabla \boldsymbol{v_1} + (\nabla \boldsymbol{v_1})^T \right] + \left(\mu_b - \frac{2}{3}\mu \right)(\nabla \cdot \boldsymbol{v_1})\mathbf{I}, \tag{11a}$$

$$\boldsymbol{f_{ac}} = -\nabla \cdot \langle \boldsymbol{\Pi} \rangle. \tag{11b}$$

The time-averaged acoustic momentum flux density tensor is defined as $\langle \boldsymbol{\Pi} \rangle = \langle p_2 \rangle \mathbf{I} + \langle \rho_0 \boldsymbol{v_1} \boldsymbol{v_1} \rangle$, p_2 is the second-order mean Eulerian pressure defined by first-order acoustic fields and is given as[22]

$$\langle p_2 \rangle = \frac{1}{4} \kappa_0 |p_1|^2 - \frac{1}{4} \rho_0 |\boldsymbol{v_1}|^2. \tag{12}$$

Therefore, the acoustic body force $\boldsymbol{f_{ac}}$ depends on the gradients in compressibility and density, the acoustic pressure, and the acoustic velocity. Fluid inhomogeneities can arise from various factors such as temperature gradients, concentration gradients, and external forces. When inhomogeneities are created by a temperature field T, $\boldsymbol{f_{ac}}$ can be expressed as[9]

$$\boldsymbol{f_{ac}} = -\frac{1}{4}|p_1|^2 \nabla \kappa_0 - \frac{1}{4}|\boldsymbol{v_1}|^2 \nabla \rho_0$$
$$= -\frac{1}{4} \left[|p_1|^2 \left(\frac{\partial \kappa}{\partial T} \right)_{T_0} + |\boldsymbol{v_1}|^2 \left(\frac{\partial \rho}{\partial T} \right)_{T_0} \right] \nabla T_0. \tag{13}$$

Both compressibility and density decrease with temperature, thus $\boldsymbol{f_{ac}}$ points toward the high temperature region. At room temperature, $\kappa |p_1|^2 \approx \rho |\boldsymbol{v_1}|^2$ and $1/\kappa \left| \frac{\partial \kappa}{\partial T} \right| \gg 1/\rho \left| \frac{\partial \rho}{\partial T} \right|$, so $\boldsymbol{f_{ac}}$ is dominated by the $|p_1|^2$ compressibility term and is, thus, the strongest at the pressure antinodes.

B. Forces on nanoparticles

The forces acting on nanoparticles include the thermophoretic force, drag force, acoustic radiation force, lift force, Brownian force, and buoyancy force. In this paper, we assume that the particles in suspension are highly diluted. Therefore, particle–particle interactions are neglected. The motion of the particle can be defined by[37–42]

$$\frac{d\boldsymbol{v_p}}{dt} = \boldsymbol{F_D} + \boldsymbol{F_T} + \boldsymbol{F_{rad}} + \boldsymbol{F_b} + \boldsymbol{F_l} + \boldsymbol{g} \left(\frac{\rho_p - \rho}{\rho_p} \right), \tag{14}$$

where $\boldsymbol{v_p}$ is the velocity of the particle, $\boldsymbol{F_D}$ is the drag force per unit particle mass, $\boldsymbol{F_T}$ is the thermophoretic force per unit particle mass, $\boldsymbol{F_{rad}}$ is the acoustic radiation force per unit particle mass, $\boldsymbol{F_b}$ is the Brownian force per unit particle mass, $\boldsymbol{F_l}$ is the Saffman's lift force per unit particle mass due to shear, and ρ_p is the particle density.

Specifically, the drag force is employed as[37]

$$\boldsymbol{F_D} = \frac{1}{\tau_p} (\boldsymbol{v} - \boldsymbol{v_p}), \tag{15a}$$

where τ_p is the particle velocity response time. Here, the Reynolds number associated with the particles' relative motion is very low, the Stokes drag law is applicable. According to the Stokes drag law, the velocity response time is given by

$$\tau_p = \frac{\rho_p d_p^2}{18\mu}, \tag{15b}$$

where d_p is the particle diameter.

The thermophoretic force is used to model the thermophoresis phenomenon, which causes particles to migrate in a fluid with a non-uniform temperature field. It is expressed by[39]

$$\boldsymbol{F_T} = \frac{6\pi\mu r_p \boldsymbol{v}}{m_p} = \frac{-6\pi\mu r_p D_T \nabla T}{m_p} = \frac{-6\pi\mu r_p S_T D \nabla T}{m_p}, \tag{16}$$

where r_p is the particle radius, and m_p is the particle mass. The Soret (S_T) coefficient is the coefficient that represents the magnitude of this

migration, and it depends on the ratio between thermodiffusion (D_T) and diffusion (D) coefficients of the system. For binary mixtures, it is expressed by $S_T = D_T/D$.

Based on the solutions to the first-order equations, the time-averaged F_{rad} on a small spherical particle, whose size is much smaller than the wavelength, can be calculated as follows:[37]

$$F_{rad} = \frac{-\pi r_p^3}{m_p} \left[\frac{2\kappa_0}{3} Re(n_1^* p_1^* \nabla p_1) - \rho_0 Re(n_2^* v_1^* \cdot \nabla v_1) \right], \quad (17a)$$

where the asterisk represents complex conjugate, and the function $Re()$ denotes the real part of the complex variable. The factors n_1 (real number) and n_2 (complex number) are

$$n_1 = 1 - \frac{\kappa_p}{\kappa_0}, \quad (17b)$$

$$n_2 = \frac{2(1-\tau)(\rho_p - \rho_0)}{2\rho_p + \rho_0(1-3\tau)}, \quad (17c)$$

$$\tau = -\frac{3}{2}\left[1 + i\left(1 + \frac{\delta}{r}\right)\right]\frac{\delta}{r}, \quad \delta = \sqrt{\frac{2\mu}{\omega\rho_0}}, \quad (17d)$$

where κ_p is the compressibility of the solid particle, and δ is the viscous boundary layer thickness in oscillatory flows.

The Brownian force is modeled as a Gaussian white noise random process given by[40]

$$F_b = \zeta\sqrt{\frac{\pi G_0}{\Delta t}} \quad \text{and} \quad G_0 = \frac{216 k_B \mu T}{\pi^2 d_p^5 \rho_p^2 C_c}, \quad (18)$$

where Δt is the time step of the simulation, $k_B = 1.380\,649 \times 10^{-23}$ J/K is the Boltzmann constant, C_c is the Stokes–Cunningham slip correction, and ζ (dimensionless) is a vector composed of zero-mean, unit-variance-independent Gaussian random numbers.

Moreover, submicrometer particles in a shear field experience a lift force perpendicular to the direction of the flow. This shear lift originates from the inertia effects in the viscous flow around the particle. For small-Reynolds number flows, it can be defined by[42]

$$F_l = \frac{2K(\mu/\rho)^{1/2}\rho}{\rho_p d_p (d_{lk} d_{kl})^{1/4}} d(v - v_p), \quad (19)$$

where $K = 2.594$, d is the deformation rate tensor, d_{lk} and d_{kl} are the deformation vector components, and k and l correspond to the unit vector in the x- and y-axis directions, respectively.

III. MODEL VERIFICATION

The first simulation is performed to verify the accuracy of the newly established acoustothermal method by comparing the current results to those published in Dumy et al.[25] All numerical simulations were conducted using COMSOL Multiphysics. The cavity used in the experiment is represented by a 2D cross-sectional rectangular domain filled with the fluid. The sidewalls are made of aluminum, the bottom wall is made of silicon and the upper wall is made of quartz. The simplified computational domain has a width $w = 4$ mm and height $h = 400\ \mu$m. The piezoelectric transducer (PZT) is actuated with a bulk acoustic wave of wavelength $\lambda = 800\mu$m and frequency $F = 1.82$ MHz. A 20 W LED source, with a 0.5 mm wide Gauss laser beam, is used as the heat source. All solid boundaries are defined as hard walls. The room temperature is taken to be 25 °C. A total of 100 polystyrene particles with a diameter of $d = 1.6\ \mu$m are tracked in the simulations. Figure 1 demonstrates the sketch of the experimental setup referred from Dumy et al.[25] As shown in Fig. 1(a), particles initially stick to each other at the elevation of 40 μm above the center of the bottom wall. Then, the bulk acoustic field is turned on with the piezoelectric substrate as shown in Fig. 1(b). Figure 1(c) illustrates that five seconds later, the LED begins heating the fluid in the middle, inducing thermal convection in water.

Figure 2 shows the results of numerical simulation. Figure 2(a) displays the first-order acoustic pressure field p_1, with the maximum amplitude equal to 1 MPa. Figure 2(b) illustrates the acoustic streaming field in the absence of the temperature gradient. Figure 2(c) demonstrates the temperature field induced by light absorption, while Fig. 2(d) demonstrates the net residual flow with the presence of the temperature gradient. When the heating source is introduced, the net
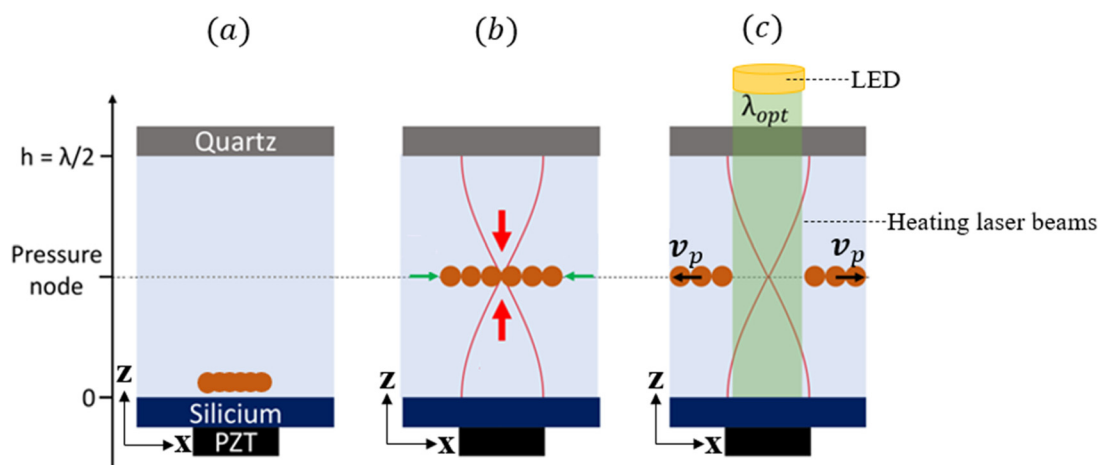
FIG. 1. The sketch of the experimental setup. (a) Sketch of the acoustic resonant cavity with microparticles at initial position (side view); (b) acoustic actuation starts at $t = 0$ s; and (c) particles in the acoustic field are heated by LED at $t = 5$ s. Reproduced with permission from Dumy et al., "Influence of the temperature on the opto-acoustophoretic effect," J. Acoust. Soc. Am. **149**(1), 556–558 (2021). Copyright 2021 Acoustical Society of America.
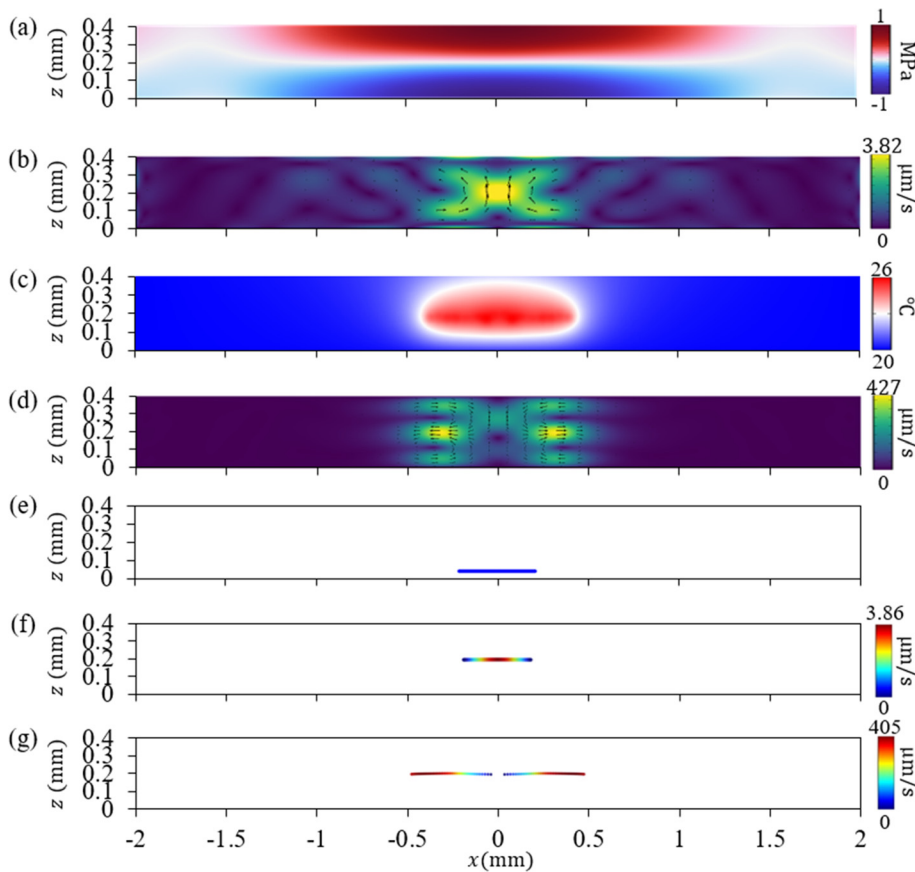
FIG. 2. Computed flow fields and particle distributions in the acoustic resonant cavity. (a) Acoustic pressure field p_1; (b) acoustic streaming field with laser off; (c) temperature field induced with laser on; (d) net residual flow with laser on; (e) initial position of particles at $t = 0$ s; (f) particles focused at the nodal plane, at $t = 5$ s; and (g) particles moved away the centerline at the nodal plane, at $t = 10$ s.

residual flow has a magnitude 100 times larger than that without the temperature gradient. There are four large re-circulations, as opposed to the flow feature of Rayleigh–Bénard convection. Two areas with large x-axis velocities appear on both sides of the z-axis centerline. Figures 2(e)–2(g) illustrate the particle distributions at different times. Figure 2(e) shows the initial position of particles at $t = 0$ s. Figure 2(f) reveals that, with the acoustic field only, the particles aggregate toward the pressure node at the mid height of the centerline just before the LED light illumination. Figure 2(g) illustrates that, as the result of the LED heating at $t = 10$ s, particles escape from the centerline toward the lower temperature region at the mid-height level. This is due to the convection toward the two sidewalls at the center area of the domain, which drags the particles in the nodal plane away from the centerline. As particles leave the heated area, the streaming flow gradually disappear. Figure 3 shows the top view of the experimental observations reported in Dumy *et al.*[25] It illustrates that, when an aggregate of spherical particles in acoustic levitation is illuminated with the input laser, the particles quickly leave the illuminated area, which has a higher temperature. The results in Fig. 3 agree well with our simulation results in Figs. 2(e)–2(g). Dumy *et al.* also mentioned that the ejection velocities were as high as a few hundred times the particles' diameter per second, which matches well with the maximum computed particle velocity of approximately 250 times their diameter per second, as shown in Fig. 2(g).[25] The thermoacoustic model used in particle manipulation is thus verified to be accurate.

IV. COMBINING ACOUSTOPHORESIS AND THERMOPHORESIS FOR PARTICLE ENRICHMENT

A. Proposed setup

In this paper, the verified model is then employed to enrich the nanoparticle with different setups for acoustic waves and the heating system. As shown in Fig. 4, the whole system comprises three parts, a 1 mm thick piezoelectrical substrate top slide, a $1000 \times 1000 \times 240\ \mu m^3$ microchamber in the middle, and a 1 mm thick sapphire bottom slide. The liquid and nanoparticle mixture are locally heated by a 1480 nm laser with a power of 194 mW, focusing on the microchamber bottom. The purpose of such a local heating setup is to generate thermal gradients, as referenced in the literature.[7,8] SSAW activated by two pairs of IDTs located on the surface of a piezoelectric substrate is introduced at the top of the microchamber. The piezoelectrical substrate is made of lithium niobate ($LiNbO_3$). The tested acoustic frequency F is 1.996 MHz (W = half wavelength) with the maximum acoustic amplitude (d_0) ranging between 0.01 and 0.5 nm. A total of 10 000 polystyrene particles, each with a radius of 50 nm, are used to represent nanovesicles.

To simplify the problem, a cross-sectional 2D model is established to represent the whole domain. The computational mesh consists of a fluid domain in the middle, and two solid domains. Figure 5 shows the central working area, which corresponds to the cross section of the microchamber in the middle.
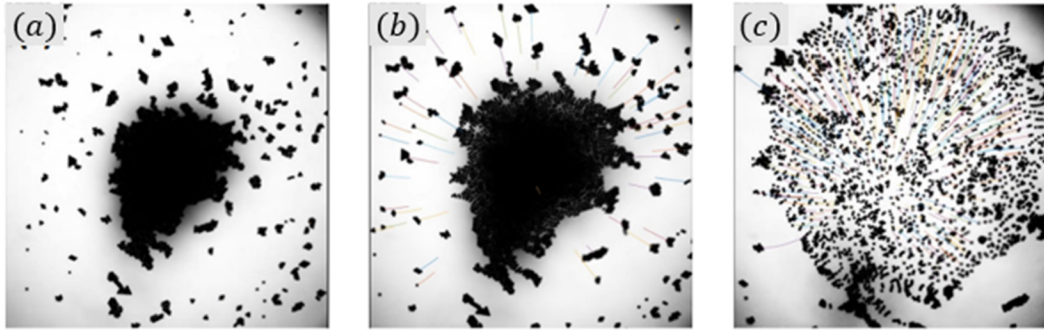
FIG. 3. The experimental results in Dumy *et al.* (a) Aggregate of spherical particles in the initial stage, (b) aggregate of spherical particles in acoustic levitation, and (c) aggregate of spherical particles was illuminated with laser power, and quickly ejected from the illuminated area. Reproduced with permission from Dumy *et al.*, "Influence of the temperature on the opto-acoustophoretic effect," J. Acoust. Soc. Am. **149**(1), 556–558 (2021). Copyright 2021 Acoustical Society of America.
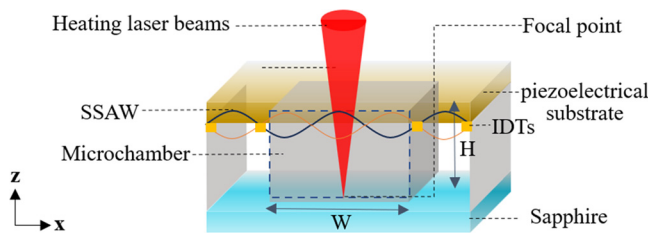
FIG. 4. Schematic of the model setup. The model consists of a microchamber sandwiched by a piezoelectrical substrate top slide, from where infrared light laser heat source and SSAW are introduced, and a sapphire bottom.

The chamber width is $W = 1000\,\mu m$ in the x direction, and the channel height is $H = 240\,\mu m$ in the z direction. The boundary conditions for the three polydimethylsiloxane (PDMS) walls, marked as Bi in Fig. 5, are modeled with an impedance wall condition given as[37]

$$\left[-p_1\mathbf{I} + \mu\left(\nabla\boldsymbol{v_1} + (\nabla\boldsymbol{v_1})^T\right) - \left(\frac{2}{3}\mu - \mu_b\right)(\nabla\cdot\boldsymbol{v_1})\mathbf{I} \right]\boldsymbol{n}$$

$$= -Z_0(\boldsymbol{n}\cdot\boldsymbol{v_1})\boldsymbol{n}, \quad (20a)$$

$$Z_0 = \rho_{PDMS} \times c_{PDMS}, \quad (20b)$$

where Z_0 is the acoustic impedance of the wall, ρ_{PDMS} and c_{PDMS} are the density and sound speed of the PDMS material, and $\boldsymbol{n}$ is an outward-pointing unit vector perpendicular to the solid surface.

The displacement function is used to model the effect of SSAW actuation at the interface between the actuation plane and the fluid, indicated as Bv in Fig. 5. For Rayleigh waves, the x- and z-components
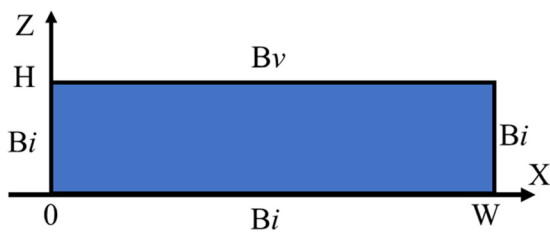

FIG. 5. Sketch of the central working area of the computational domain.

of the displacement have a phase difference of 90°, so points at the boundary undergo elliptical motion and the displacement functions can be given as[37]

$$u_x(x, t) = \xi d_0\left[e^{-C_d\left(\frac{W}{2}-x\right)}e^{i\left[-k\left(\frac{W}{2}-x\right)+\omega t\right]} + e^{-C_d\left(\frac{W}{2}+x\right)}e^{i\left[k\left(\frac{W}{2}+x\right)+\omega t\right]}\right], \quad (21a)$$

$$u_z(x,t) = -d_0\left[e^{-C_d\left(\frac{W}{2}-x\right)}e^{i\left[-k\left(\frac{W}{2}-x\right)+\omega t-\frac{\pi}{2}\right]} - e^{-C_d\left(\frac{W}{2}+x\right)}e^{i\left[k\left(\frac{W}{2}+x\right)+\omega t-\frac{\pi}{2}\right]}\right], \quad (21b)$$

where d_0 is the maximum amplitude of the z-component SSAW displacement, $k = 2\pi/\lambda$ is the wavenumber, ξ is the ratio between the x- and z-components. By differentiating Eq. (21) with respect to time, the first-order velocity imposed over Bv can be obtained. In the frequency domain analysis, the time-dependent terms are removed. Therefore, the velocity boundary condition can be given as

$$v_x(x, t) = \xi d_0\omega\left[e^{-C_d\left(\frac{W}{2}-x\right)}e^{i\left[-k\left(\frac{W}{2}-x\right)\right]} + e^{-C_d\left(\frac{W}{2}+x\right)}e^{i\left[k\left(\frac{W}{2}+x\right)\right]}\right], \quad (22a)$$

$$v_z(x, t) = -d_0\omega\left[e^{-C_d\left(\frac{W}{2}-x\right)}e^{i\left[-k\left(\frac{W}{2}-x\right)-\frac{\pi}{2}\right]} - e^{-C_d\left(\frac{W}{2}+x\right)}e^{i\left[k\left(\frac{W}{2}+x\right)-\frac{\pi}{2}\right]}\right]. \quad (22b)$$

At the walls, the fluid velocity is set to zero due to the no-slip condition on all the boundaries of the microchannel, consistent with previous studies.[36,37] In particle trajectories calculation, both sticky and repulsive wall conditions have been tested in our simulations, but they demonstrate highly similar results in predicting the particle trajectories. In implementing the sticky wall condition, when a particle hits the wall, its position is frozen and its velocity is set to zero. In the repulsive wall condition, elastic collision is assumed when a particle hits the wall, so the normal velocity reverses and the tangential velocity is unchanged. Experimental observations indicate that cells typically adhere to the solid surfaces upon contact.[7,8] Given the intended connection between our simulations and the biological and medical applications, only the results with the sticky wall condition are presented in this paper.

In all the tested cases, the background temperature is taken to be $T = 25\,°C$. At this temperature, the key properties of water are $\rho_0 = 997\,kg/m^3$, $\mu = 0.890$ mPa s, $\mu_b = 2.47$ mPa s, $\kappa_0 = 448$ T/Pa, and the spend of sound in water $c_0 = 1497\,m/s$; the values of the key parameters of polystyrene are $\rho_p = 1050\,kg/m^3$, $\kappa_p = 249$ T/Pa, and the spend of sound in polystyrene $c_{ps} = 2350\,m/s$; the key properties of PDMS (10:1) are $\rho_{PDMS} = 920\,kg/m^3$, and speed of sound

30 September 2024 11:24:06

$c_{PDMS} = 1076.5$ m/s.[43–48] The thermal conductivities k of water, LiNbO$_3$, and sapphire are 0.6, 56, and 35 W m^{-1}K^{-1}, respectively. The heat capacities c_p of water, LiNbO3 and sapphire are 4200, 628, and 755 J Kg^{-1}K^{-1}, respectively.[7,8] The decay coefficient C_d is calculated based on the leaky SSAW dispersion relationship detailed in Vanneste and Bühler.[49]

The solver consists of four steps: (a) Determining the temperature field T_0 induced by the laser heating; (b) Computing the acoustic velocity v_1 in the solid and the pressure p_1 in the fluid due to actuation on the piezoelectric substrate in the frequency domain; (c) Computing the resulting stationary streaming field v_2; and (d) Calculating the resultant force exerted on the nanoparticles, and to determine the velocity and displacement of nanoparticles. Adequate mesh resolution is ensured for an accurate representation of the governing equations in the domain, while maintaining computational efficiency.

B. Numerical simulation

Based on the previous setup and governing equations, the temperature field is presented in Fig. 6(a), with temperatures ranging from 25 to 57 °C on the x–z plane. Laser irradiation resulted in a heated core in the center of the microchamber and formed a cold region at the chamber bottom beneath the heated core. Figures 6(b) and 6(c) show typical acoustic field and flow field with the maximum amplitude of SSAW displacement $d_0 = 0.109$ nm. In Fig. 6(b), the acoustic waves introduced at the top boundary propagate downward, and the maximum amplitude of the first-order pressure oscillation is 6.81 kPa. In Fig. 6(c), the fluid velocity field exhibits magnitudes ranging from 0 to 27 μm/s. A toroidal convection converges near the microchamber bottom but diverges near the microchamber top.

After defining the flow field and temperature distribution, the particle tracing module is employed to compute the accumulation process of the nanoparticles. To facilitate the analyses of nanoparticle accumulation, a target box is setup with a diameter of 100μm and a height of 5 μm, as shown in Fig. 7. The time taken by the nanoparticles
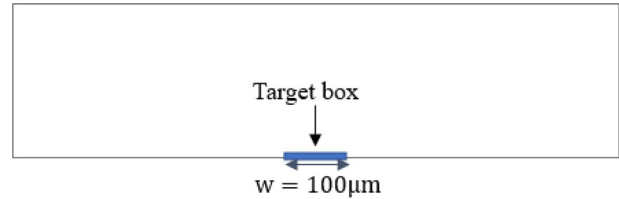
FIG. 7. Schematic of the target box with a diameter of 100 μm and a height of 5 μm.

to reach a steady state is defined as t_d, and the percentage of particles in the box at the steady state was denoted as p^∞. Figure 8(a) presents the initial positions of nanoparticles. Figure 8(b) demonstrates that with the acoustic field presented in Fig. 6(b), all of the nanoparticles move into the target box and reach the final position. Even when incorporating SSAW, the nanoparticles are still dominated by the thermophoretic force and drag force, while the acoustophoretic radiation force and other forces are several orders of magnitude smaller than these dominating forces. Thermophoresis pushes particles away from the hot region, while thermal convection flow drags particles toward the center of the chamber bottom. Particles in the lower half of the fluid chamber, therefore, experience a Stokes force dragging them toward the center of the chamber bottom and a thermophoretic force pushing them away, with their individual trajectories resulting from the combined action of these forces.

V. RESULTS AND DISCUSSION

A. The influence of acoustic field on the nanoparticle enrichment

This section uses the validated model to study the influence of the acoustic field on the nanoparticle enrichment time. In this study, a total of 26 maximum acoustic amplitudes (d_0) ranging from 0 to 0.5 nm are tested. Figure 9 demonstrates that the maximum magnitude of the first-order pressure p_1 (p_{1max}) is proportional to d_0. Figure 10 presents the flow field with different d_0. In Fig. 10(a), with only a temperature gradient, the fluid velocity field exhibits magnitudes ranging from 0 to 60 μm/s. A toroidal convection converges near the microchamber bottom but diverges near the microchamber top. Figure 10(b) employs the thermoacoustic streaming induced from
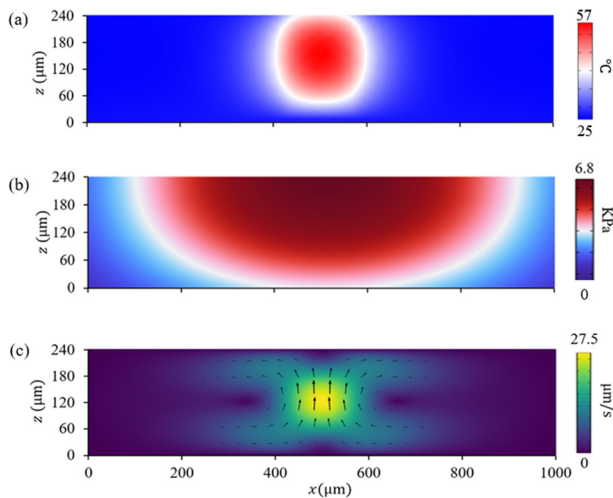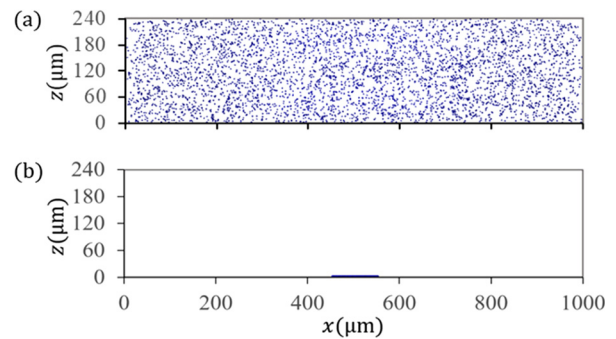

FIG. 6. Numerical simulation results. (a) Temperature field; (b) first-order pressure field p_1, with $F = 1.996$ MHz and $d_0 = 0.109$ nm; and (c) time-averaged second-order velocity field $\langle v_2 \rangle$, with $d_0 = 0.109$ nm.

FIG. 8. Particle accumulation progress. (a) Initial distribution of particles and (b) particles reaching final positions.

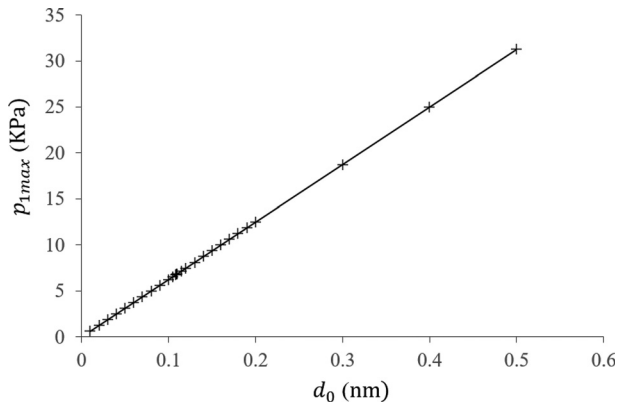**FIG. 9.** Relationship between p_{1max} and d_0.

FIG. 11. p_{1max} vs maximum time-averaged second-order velocity $\langle v_2 \rangle$.

acoustic field with $F = 1.996$ MHz and $d_0 = 0.109$ nm, which exhibits a fluid velocity field with magnitudes ranging from 0 to 27.5 μm/s. The velocity field is similar to the one without SSAW but has a lower magnitude. With a small amplitude of acoustic pressure, the acoustic streaming induced by f_{ac} is not strong enough to change the convection direction. However, with an increase in maximum acoustic amplitude (i.e., $d_0 = 0.5$ nm), the convection starts to move in the opposite direction as shown in Fig. 10(c). It diverges near the microchamber top and converges near the microchamber bottom, with a large velocity magnitude primarily due to the increased nondissipative f_{ac}. In this case, the pressure is stronger at the top of the microchamber, resulting in a stronger f_{ac} at the top. Consequently, in the upper part of the heat core, f_{ac} pushes the fluid horizontally inward to the center, moving it downward along the z-axis direction. Due to mass conservation, the fluid is then forced to flow outward along the axial x direction.
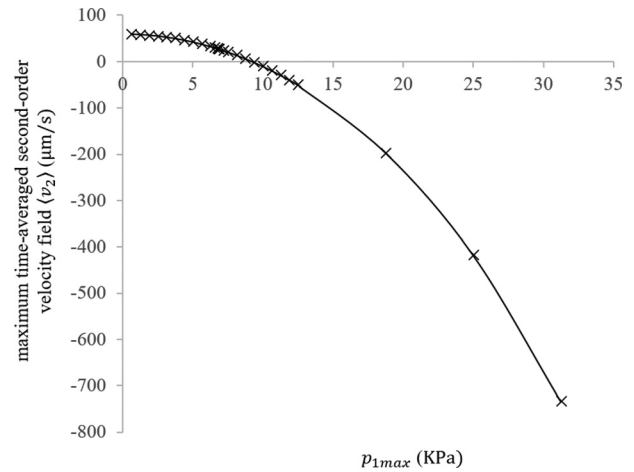
Figure 11 shows the relationship between the maximum amplitude of the first-order pressure p_1 and maximum time-averaged second-order velocity field $\langle v_2 \rangle$. With the same temperature gradient, when p_{1max} increases from 0, the coupling of SSAW can gradually reduce the thermal convection induced by local heating until it reaches a threshold p_{1max}. At this point, $\langle v_2 \rangle$ approaches 0 and the convection direction changes. Subsequently, the maximum magnitude of $\langle v_2 \rangle$ continuously increases to a significant value with p_{1max} in the opposite direction, driven by a temperature gradient-induced nondissipative acoustic body force.

It is observed from results that the nanoparticle accumulation performance varied with different acoustic field amplitudes. To illustrate this, the particle trajectories with three different p_{1max} values at
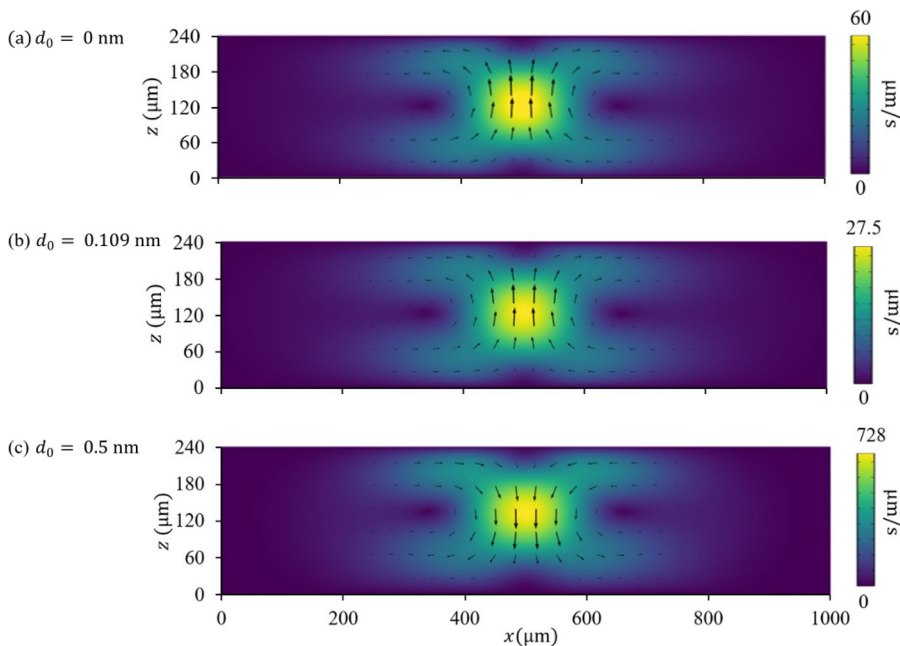

FIG. 10. Time-averaged second-order velocity field $\langle v_2 \rangle$, at different d_0.

10, 20, 30, and 40 s are presented in Figs. 12, 13, and 14, respectively. In Fig. 12, when $p_{1max} = 0.63$ KPa, nanoparticles are pushed away from the hot region and follow the convection flow toward the center of the chamber bottom. Due to the large streaming velocity in the middle area, some particles are redirected upward as they approach the center of the microchamber bottom, and then move away from the center of the microchamber. After traveling a certain distance, these particles move down toward the substrate and repeat this pattern continuously. With the passage of tested time, more particles stabilize at the center of the chamber bottom, while fewer particles travel with the convection flow. Although all the particles eventually reach the target box, the circulation phenomenon of nanoparticles increases the time needed to reach their final positions. As p_{1max} increases, the streaming velocity gradually decreases, thereby reducing the circulation phenomenon. Figure 13 demonstrates that when $p_1 = 6.8$ kPa, the circulation phenomenon of particles has been largely reduced. Although the maximum velocity of particles reduces, nanoparticles can achieve faster aggregation to the final position. As the maximum amplitude of p_1 increases from $p_{1max} = 6.8$ kPa, the circulation phenomenon gradually disappears due to the continuous reduction of streaming velocity. As shown in Fig. 14, when $p_{1max} = 8.8$ kPa, the circulation phenomenon disappears. but the maximum velocity of particle movement experiences a significant decrease to $4.3\ \mu m/s$, resulting in an increased particle enrichment time. As the maximum amplitude of p_1 continues to increase from 8.8 kPa, in the lower half of the fluid chamber, the Stokes force is no longer strong enough to drag nanoparticles toward the center of the chamber bottom, and the thermophoretic force pushes them away from the center, significantly reducing aggregation efficiency. Figure 15 demonstrates the variation in the percentages of 100 nm particles arriving at designated positions with these three different p_{1max} values.

Figure 16 shows the speed of nanoparticle aggregation with all the tested p_{1max}. The enrichment time first reduces as p_{1max} increases,
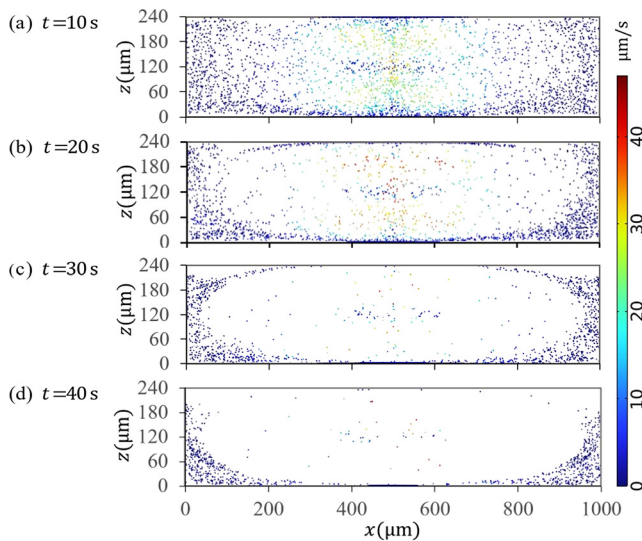

FIG. 13. Particle trajectories at different times with $p_{1max} = 6.8$ kpa; the circulation phenomenon of particles has been largely reduced.

until it reaches the minimum value of $t_d = 33$ s when p_{1max} equals 6.8 KPa. Then t_d gradually extends as p_{1max} increases further. After p_{1max} reaches 8.8 kPa, it begins to drive the convection moves in the opposite direction, nanoparticles are pushed away from the bottom center and particle accumulation cannot be achieved. The results indicate that by properly applying SSAW with a small magnitude of p_{1max}, a reduction of t_d can be realized. Consequently, by incorporating optimum $p_{1max} = 6.8$ kPa, which balance the function of thermophoresis and thermal conduction flow, the nanoparticle enrichment time can

FIG. 12. Particle trajectories at different times with $p_{1max} = 0.63$ kPa; the circulation phenomenon of nanoparticles increases the time needed to reach their final positions.

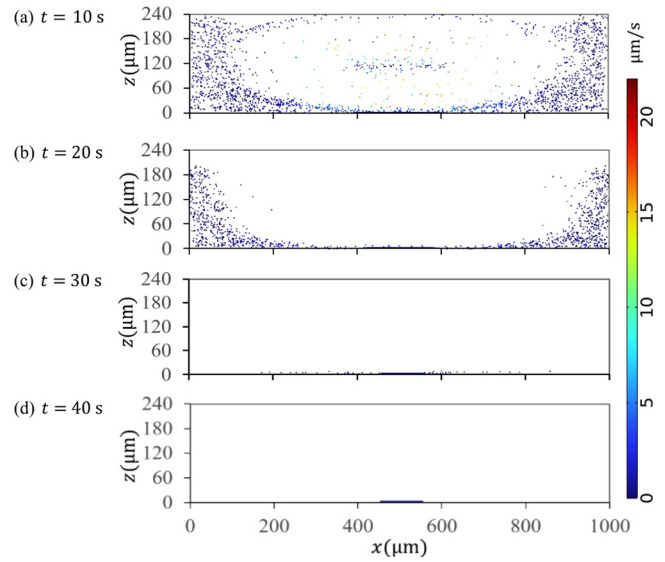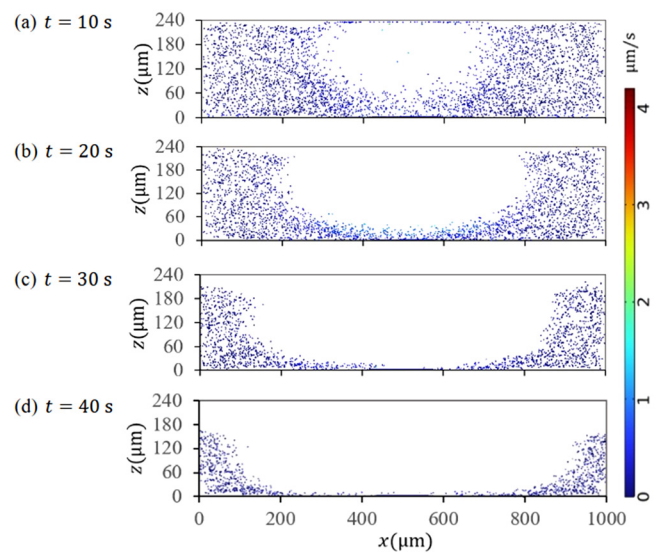**FIG. 14.** Particle trajectories at different times with $p_{1max} = 8.8$ kpa; the maximum velocity of particle movement experiences a significant decrease.
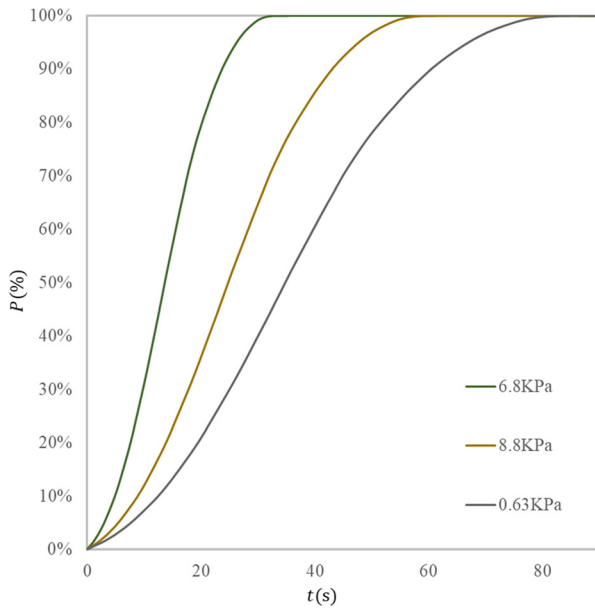
FIG. 15. Percentages of 100 nm particles arriving at designated position, at three typical $p_{1max} = 0.63, 6.8$, and 8.8 kPa.

be reduced by about 61% compared to the thermophoresis enrichment without an acoustic field.

B. The variation of optimum p_{1max} with laser power

In Sec. V A, the influence of the acoustic field on the nanoparticle accumulation is investigated with a 32°C temperature difference induced by 194 mw laser power. It is valuable to know the feasibility of the time reduction by acoustophoresis for different laser powers. This section, therefore, tested the sensitivity of the acoustic field to the variation of laser powers from 194 to 248mW, which corresponds to temperature differences ranging from 32 to 41 °C. The target box and t_d are defined as the same as those in Sec. IV B. Using the COMSOL
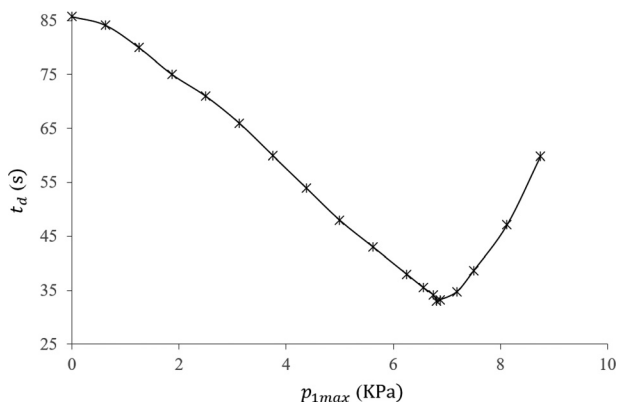

FIG. 16. Time of particle aggregation vs p_{1max}; with optimum $p_{1max} = 6.8$ kPa, the minimum value of $t_d = 33$ s can be achieved.

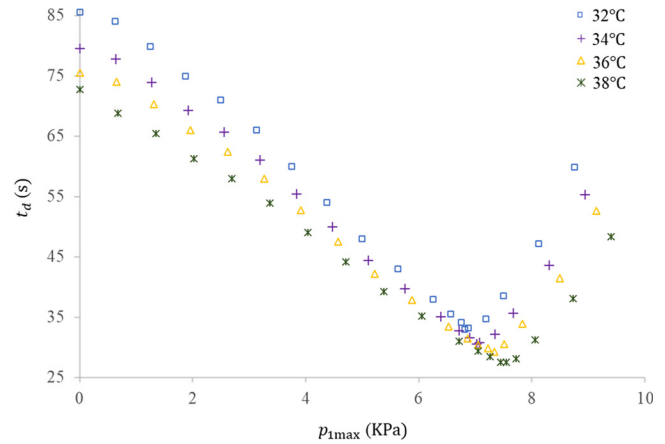**FIG. 17.** Nanoparticle enrichment time vs p_{1max} for selected $\Delta T = 32, 34, 36$, and 38 °C. The nanoparticle enrichment times all reduce with the increase in p_{1max} until they reach an optimum value of p_{1max}.

Material Library, the values of material properties and their temperature dependence are considered in the simulation.

There are ten temperature differences (ΔT) tested in total, but only four are presented to describe the key findings, as shown in Fig. 17. Different ∇T exhibit similar performance in the variation of nanoparticle enrichment time with the change in p_{1max}. The nanoparticle enrichment times all reduce with the increase in p_{1max} until they reach an optimum value of p_{1max}. When p_{1max} increases beyond the optimum value, t_d extends again. With the optimum value of p_{1max}, t_d for all the tested ΔT, we observe a significant reduction of approximately 61% when compared to nanoparticle enrichment with only thermophoretic effect. Figure 18 shows that the optimum p_{1max} increases from 6.8 to 7.9 kPa as the ΔT increases from 32 to 41 °C, corresponding to a 16% increase in p_{1max} with a 10 °C increase in ΔT. This is attributed to the fact that the maximum magnitude of thermal convection velocity increases with ΔT. Consequently, a stronger amplitude of acoustic field is required to counterbalance the increasing convection velocity, thereby achieving an optimum condition for nanoparticle enrichment.

VI. CONCLUSIONS

This paper has developed a novel nanoparticle enrichment method that couples thermophoresis and acoustophoresis. An IR laser is used to generate the temperature gradient, and the microchamber is sandwiched between a LiNbO3 top slide and a sapphire bottom slide. SSAW is introduced from the top of the microchamber. The motion of nanoparticles is primarily governed by the thermophoretic force and the drag force, while the acoustophoretic force becomes negligible for nanosized particles.

A finite element model is established to verify the effectiveness of the proposed model, which has been validated against a past case study, confirming its reliability and accuracy. In the parametric study, the laser power is fixed at 194 mW, and the input SSAW has a frequency F of 1.996 MHz with an acoustic amplitude (d_0) ranging from 0.01 and 0.5 nm. When SSAW is actuated from the top of the microchamber, the induced acoustic streaming can be controlled to occur in the direction opposite to natural heat convection. As p_{1max} increases,
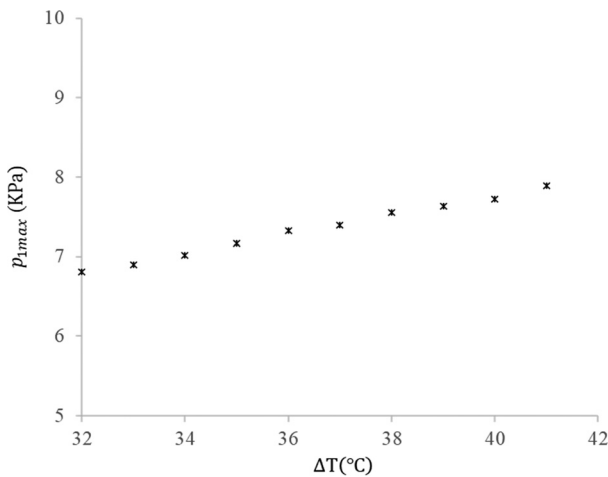
FIG. 18. Optimum values of p_{1max} increase from 6.8 to 7.9 kPa as the tested ΔT increase from 32 to 41 °C.

the velocity of acoustic streaming gradually increases to the same magnitude of v_0 and then the residual flow reverses. After that, the magnitude of residual flow can continuously increase to over 10 times larger than that caused by heat convection alone. The results reveal that SSAW has a significant influence on nanoparticle accumulation efficiency. With the current configuration, the study suggests that, by integrating SSAW with an optimum p_{1max} of 6.8 kPa, the accumulation time of nanoparticles can be shortened by about 61%.

Further investigations are conducted to study the sensitivity of the conclusions to the variation of input laser power ranging from 194 to 248 mW, corresponding to the temperature difference ranging from 32 to 41 °C, respectively. It is found that a reduction in the nanoparticle enrichment time by approximately 61% can be achieved in all these tested cases. With the increased strength of thermal convection, the optimum amplitude of the actuated acoustic pressure increases slightly from 6.8 to 7.9 kPa. These findings further prove the feasibility of the proposed enrichment method and gain insight into the design of nanoparticle enrichment devices.

AUTHOR DECLARATIONS
Conflict of Interest

The authors have no conflicts to disclose.

Author Contributions

Jing Dong: Conceptualization (lead); Data curation (lead); Formal analysis (lead); Investigation (equal); Methodology (lead); Project administration (lead); Resources (equal); Software (lead); Validation (lead); Visualization (lead); Writing – original draft (lead); Writing – review & editing (lead). **Dongfang Liang:** Conceptualization (equal); Methodology (equal); Project administration (equal); Resources (equal); Supervision (lead); Validation (equal); Visualization (equal); Writing – review & editing (equal). **Alexandre J. Kabla:** Methodology (equal); Supervision (equal); Visualization (equal); Writing – review & editing (equal). **Xinan Chen:** Investigation (equal); Resources (equal); Software (equal); Writing – review & editing (equal). **Xin Yang:** Conceptualization (equal); Methodology (equal); Resources (equal); Supervision (equal); Writing – review & editing (equal).

DATA AVAILABILITY

The data that support the findings of this study are available from the corresponding author upon reasonable request.

REFERENCES

[1] Z. Mao, P. Li, M. Wu, H. Bachman, N. Mesyngier, X. Guo, S. Liu, F. Costanzo, and T. J. Huang, "Enriching nanoparticles via acoustofluidics," ACS Nano **11**, 603–612 (2017).

[2] K. Lee, H. Shao, R. Weissleder, and H. Lee, "Acoustic purification of extracellular microvesicles," ACS Nano **9**, 2321–2327 (2015).

[3] D. J. Collins, T. Alan, and A. Neild, "Particle separation using virtual deterministic lateral displacement (vDLD)," Lab Chip **14**(9), 1595–1603 (2014).

[4] Y. Gu, C. Chen, Z. Mao, H. Bachman, R. Becker, J. Rufo, Z. Wang, P. Zhang, J. Mai, S. Yang, J. Zhang, S. Zhao, Y. Ouyang, D. T. W. Wong, Y. Sadovsky, and T. J. Huang, "Acoustofluidic centrifuge for nanoparticle enrichment and separation," Sci. Adv. **7**, eabc0467 (2021).

[5] H. Wu, Z. Tang, R. You, S. Pan, W. Liu, H. Zhang, T. Li, Y. Yang, C. Sun, W. Pang, and X. Duan, "Manipulations of micro/nanoparticles using gigahertz acoustic streaming tweezers," Nanotechnol. Precis. Eng. **5**, 023001 (2022).

[6] W. Wei, Z. Wang, B. Wang, X. He, Y. Wang, Y. Bai, Q. Yang, W. Pang, and X. Duan, "Acoustofluidic manipulation for submicron to nanoparticles," Electrophoresis **1**, 1–22 (2024).

[7] C. Liu, J. Zhao, F. Tian, L. Cai, W. Zhang, Q. Feng, J. Chang, F. Wan, Y. Yang, B. Dai, Y. Cong, B. Ding, J. Sun, and W. Tan, "Low-cost thermophoretic profiling of extracellular-vesicle surface proteins for the early detection and classification of cancers," Nat. Biomed. Eng. **3**, 183–193 (2019).

[8] J. Zhao, C. Liu, Y. Li, Y. Ma, J. Deng, L. Li, and J. Sun, "Thermophoretic detection of exosomal microRNAs by nanoflares," J. Am. Chem. Soc. **142**, 4996–5001 (2020).

[9] W. Qiu, J. H. Joergensen, E. Corato, H. Bruus, and P. Augustsson, "Fast microscale acoustic streaming driven by a temperature-gradient-induced nondissipative acoustic body force," Phys. Rev. Lett. **127**, 064501 (2021).

[10] L. Rayleigh, "On waves propagated along the plane surface of an elastic solid," Proc. London Math. Soc. **s1-17**, 4–11 (1885).

[11] X. Ding, P. Li, S. C. Lin, Z. S. Stratton, N. Nama, F. Guo, D. Slotcavage, X. Mao, J. Shi, F. Costanzo, and T. J. Huang, "Surface acoustic wave microfluidics," Lab Chip **13**, 3626–3649 (2013).

[12] S. Li, X. Ding, F. Guo, Y. Chen, M. I. Lapsley, S.-C. S. Lin, L. Wang, J. P. McCoy, C. E. Cameron, and T. J. Huang, "An on-chip, multichannel droplet sorter using standing surface acoustic waves," Anal. Chem. **85**, 5468–5474 (2013).

[13] A. Riaud, M. Baudoin, O. Bou Matar, J.-L. Thomas, and P. Brunet, "On the influence of viscosity and caustics on acoustic streaming in sessile droplets: An experimental and a numerical study with a cost-effective method," J. Fluid Mech. **821**, 384 (2017).

[14] H. Dong, M. Sui, G. Mu, J. Zhao, T. Li, T. Sun, and K. T. V. Grattan, "Velocity and direction adjustment of actuated droplets using the standing wave ratio of surface acoustic waves (SAW)," IEEE/ASME Trans. Mechatron. **28**, 2399–2404 (2023).

[15] N. S. Satpathi, K. N. Nampoothiri, and A. K. Sen, "Effects of surface acoustic waves on droplet impact dynamics," J. Colloid Interface Sci. **641**, 499–509 (2023).

[16]M. Sui, H. Dong, G. Mu, J. Xia, J. Zhao, Z. Yang, T. Li, T. Sun, and K. Grattan, "Droplet transportation by adjusting the temporal phase shift of surface acoustic waves in the exciter–exciter mode," Lab Chip **22**, 3402–3411 (2022).

[17]Y. Chen, M. Wu, L. Ren, J. Liu, P. H. Whitley, L. Wang, and T. J. Huang, "High-throughput acoustic separation of platelets from whole blood," Lab Chip **16**, 3466–3472 (2016).

[18]D. Xu, F. Cai, M. Chen, F. Li, C. Wang, L. Meng, D. Xu, W. Wang, J. Wu, and H. Zheng, "Acoustic manipulation of particles in a cylindrical cavity: Theoretical and experimental study on the effects of boundary conditions," Ultrasonics **93**, 18–25 (2019).

[19]S. Zhao, M. Wu, S. Yang, Y. Wu, Y. Gu, C. Chen, J. Ye, Z. Xie, Z. Tian, H. Bachman, P. H. Huang, J. Xia, P. Zhang, H. Zhang, and T. J. Huang, "A disposable acoustofluidic chip for nano/microparticle separation using unidirectional acoustic transducers," Lab Chip **20**, 1298–1308 (2020).

[20]S. Ning, S. Liu, Y. Xiao, G. Zhang, W. Cui, and M. Reed, "A microfluidic chip with a serpentine channel enabling high-throughput cell separation using surface acoustic waves," Lab Chip **21**, 4608–4617 (2021).

[21]H. Wang, J. Boardman, X. Zhang, C. Sun, M. Cai, J. Wei, Z. Dong, M. Feng, D. Liang, S. Hu, Y. Qian, S. Dong, Y. Fu, H. Torun, A. Clayton, Z. Wu, Z. Xie, and X. Yang, "An enhanced tilted-angle acoustic tweezer for mechanical phenotyping of cancer cells," Anal. Chim. Acta **1255**, 341120 (2023).

[22]J. T. Karlsen, P. Augustsson, and H. Bruus, "Acoustic force density acting on inhomogeneous fluids in acoustic fields," Phys. Rev. Lett. **117**, 114504 (2016).

[23]J. H. Joergensen, W. Qiu, and H. Bruus, "Transition from boundary-driven to bulk-driven acoustic streaming due to nonlinear thermoviscous effects at high acoustic energy densities," Phys. Rev. Lett. **130**, 044001 (2023).

[24]G. Dumy, M. Hoyos, and J. L. Aider, "Observation of selective optical manipulation of particles in acoustic levitation," J. Acoust. Soc. Am. **146**(1), 4557 (2019).

[25]G. Dumy, M. Hoyos, and J. L. Aider, "Influence of the temperature on the opto-acoustophoretic effect," J. Acoust. Soc. Am. **149**(1), 556–558 (2021).

[26]W. Qiu, H. Bruus, and P. Augustsson, "Particle-size-dependent acoustophoretic motion and depletion of micro-and nano-particles at long timescales," Phys. Rev. E **102**, 013108 (2020).

[27]D. Van Assche, E. Reithuber, W. Qiu, T. Laurell, B. Henriques-Normark, P. Mellroth, P. Ohlsson, and P. Augustsson, "Gradient acoustic focusing of submicron particles for separation of bacteria from blood lysate," Sci. Rep. **10**, 3670 (2020).

[28]J. P. Koulakis, S. Pree, A. L. F. Thornton, and S. Putterman, "Trapping of plasma enabled by pycnoclinic acoustic force," Phys. Rev. E **98**, 043103 (2018).

[29]D. A. Drew, "Mathematical modeling of two-phase flow," Annu. Rev. Fluid Mech. **15**, 261–291 (1983).

[30]P. Kr. Das, A. D. Snider, and V. R. Bhethanabotla, "Acoustothermal heating in surface acoustic wave driven microchannel flow," Phys. Fluids **31**, 106106 (2019).

[31]V. Kumar, M. Azharudeen, C. Pothuri, and K. Subramani, "Heat transfer mechanism driven by acoustic body force under acoustic fields," Phys. Rev. Fluids **6**, 073501 (2021).

[32]J. Dong, D. Liang, X. Chen, and X. Yang, "Influences of laser heating parameters on thermophoretic enrichment of nanoparticles," Int. J. Heat Mass Transfer **218**, 124765 (2024).

[33]W. L. Nyborg, "Acoustic streaming," in *Nonlinear Acoustics*, edited by M. F. Hamilton and D. T. Blackstock (Academic Press, 1998), pp. 207–231.

[34]W. L. Nyborg, "Acoustic streaming," in *Physical Acoustics*, edited by W. P. Mason and R. N. Thurston (Academic Press, New York, 1965), pp. 265–329.

[35]J. H. Joergensen and H. Bruus, "Theory of pressure acoustics with thermoviscous boundary layers and streaming in elastic cavities," J. Acoust. Soc. Am. **149**, 3599–3610 (2021).

[36]P. B. Muller, R. Barnkob, M. J. H. Jensen, and H. Bruus, "A numerical study of microparticle acoustophoresis driven by acoustic radiation forces and streaming-induced drag forces," Lab Chip **12**, 4617–4627 (2012).

[37]J. Dong, D. Liang, X. Yang, and C. Sun, "Influences of microparticle radius and microchannel height on SSAW-based acoustophoretic aggregation," Ultrasonics **117**, 106547 (2021).

[38]J. L. Anderson, "Colloid transport by interfacial forces," Annu. Rev. Fluid Mech. **21**, 61–99 (1989).

[39]W. Li and E. J. Davis, "Measurement of the thermophoretic force by electrodynamic levitation: Microspheres in air," J. Aerosol Sci. **26**, 1063–1083 (1995).

[40]J. R. Bielenberg and H. Brenner, "A hydrodynamic/Brownian motion model of thermal diffusion in liquids," Physica A **356**, 279–293 (2005).

[41]A. Guha, "Transport and deposition of particles in turbulent and laminar flow," Annu. Rev. Fluid Mech. **40**, 311–341 (2008).

[42]P. G. Saffman, "The lift on a small sphere in a slow shear flow," J. Fluid Mech. **22**, 385–400 (2006).

[43]J. K. Tsou, J. Liu, A. I. Barakat, and M. F. Insana, "Role of ultrasonic shear rate estimation errors in assessing inflammatory response and vascular risk," Ultrasound Med. Biol. **34**, 963–972 (2008).

[44]M. J. Holmes, N. G. Parker, and M. J. W. Povey, "Temperature dependence of bulk viscosity in water using acoustic spectroscopy," J. Phys.: Conf. Ser. **269**, 012011 (2011).

[45]L. D. Landau, E. M. Lifshitz, A. M. Kosevich, J. B. Sykes, L. P. Pitaevskii, and W. H. Reid, *Theory of Elasticity* (Elsevier Science, 1986), Vol. 7.

[46]D. Armani, C. Liu, and N. Aluru, "Re-configurable fluid circuits by PDMS elastomer micromachining," in *Technical Digest. IEEE International MEMS 99 Conference. Twelfth IEEE International Conference on Micro Electro Mechanical Systems (Cat. No. 99CH36291)* (IEEE 1999), pp. 222–227.

[47]*CRC Handbook of Chemistry and Physics*, 92nd ed., edited by W. M. Haynes (Taylor and Francis Group, 2012).

[48]L. Bergmann, *Der Ultraschall Und Seine Anwendung in Wissenschaft Und Technik*, 6th ed. (S. Hirzel Verlag, Stuttgart, 1954).

[49]J. Vanneste and O. Bühler, "Streaming by leaky surface acoustic waves," Proc. R. Soc. A **467**, 1779–1800 (2011).